Journal of the Optical Society of America B

OPTICAL PHYSICS

Low-threshold supercontinuum generation in polycrystalline media

Sergey Vasilyev,[1,5] **Jiahui Gu,**[2] **Mike Mirov,**[1] **Yury Barnakov,**[1] **Igor Moskalev,**[1] **Viktor Smolski,**[1] **Jeremy Peppers,**[1] **Miroslav Kolesik,**[2,6] **Sergey Mirov,**[1,3] **and Valentin Gapontsev**[4]

[1]*IPG Photonics—Southeast Technology Center, Birmingham, Alabama 35211, USA*
[2]*College of Optical Sciences, University of Arizona, Tucson, Arizona 85721, USA*
[3]*Department of Physics, University of Alabama at Birmingham, Birmingham, Alabama 35294, USA*
[4]*IPG Photonics Corporation, 50 Old Webster Rd., Oxford, Massachusetts 01540, USA*
[5]*e-mail: svasilyev@ipgphotonics.com*
[6]*e-mail: kolesik@acms.arizona.edu*

Until recently, the generation of super-octave continua in bulk materials at full repetition rates of femtosecond (fs) oscillators has been limited to a few special cases of Kerr lens mode-locked Ti:sapphire lasers. In 2019, we described a 3.4-octave fs source with 50 nJ pulse energy at the repetition rate of 78 MHz based on polycrystalline Cr:ZnS [Vasilyev *et al.*, Optica6, 126 (2019)]. Here we explain the mechanism of fs supercontinuum generation in transition-metal doped polycrystalline II-VI semiconductors at relatively low (nJ-level) pulse energy. We demonstrate that this new supercontinuum regime is enabled by a complex, yet well-reproducible, interplay between the effects arising from the third-order nonlinearity, the quadratic nonlinearities, and thermal optical effects in the medium. We also demonstrate the control of fs pulse propagation in disordered $\chi^{(2)}$ media via the control of the material microstructure. © 2021 Optical Society of America under the terms of the OSA Open Access Publishing Agreement

https://doi.org/10.1364/JOSAB.417485

1. INTRODUCTION

Supercontinuum generation (SCG) is one of the most exciting subjects of nonlinear optics with many applications in science, technology, medicine, and industry [1]. In particular, SCG with fs pulses (fs SCG) attracts attention because it yields optical spectra that combine a broad, super-octave bandwidth with a high spatial and temporal coherence. Therefore, fs SCG is crucial for a number of important applications; e.g., the generation of optical frequency combs [2], arbitrary optical waveform synthesis [3], and generation of attosecond pulses [4], to name but a few. The techniques for SCG in optical fibers [5–7], waveguides [8,9], and bulk dielectrics and semiconductors [10] are now well established. Guided geometries enable SCG at low (pJ-to-nJ level) pulse energies and provide the possibilities to tailor the dispersive properties of the device. On the other hand, the implementations of bulk fs SCG are most straightforward: One merely has to focus a laser beam in a piece of nonlinear material, but they require fs lasers with relatively high (μJ-level) pulse energy that typically operate at kHz repetition rates.

There have been a number of recent reports on fs SCG in optical materials with a high second-order nonlinearity. In this regime, the conventional spectral broadening, which arises from $\chi^{(3)}$, is augmented by intrapulse, three-wave mixings, and the

effective nonlinear index n_2 is modified by cascaded quadratic nonlinearities (CQN) [11,12]. Thus, the second-order nonlinearity provides interesting opportunities for the control of fs pulse propagation in the medium, as has been demonstrated in bulk [12–20] and in confined geometries [21,22]. Importantly, the use of structured bulk $\chi^{(2)}$ materials has enabled special regimes where the fs SCG occurs at a relatively low (nJ-level) energy of pulses at full repetition rate of a fs oscillator (f_R). This low-threshold bulk SCG regime is appealing because of its simplicity, alignment insensitivity, and power-scaling capabilities.

In their recent report [20], Rutkauskas *et al*. provide an example of a low-threshold bulk SCG in a quasi-phase-matched (QPM) material, an orientation-patterned gallium phosphide. The visible (blue/green to red) SCG was obtained from the near-IR pulse train (1.04 μm, 30-cycle, 32 nJ at $f_R = 100$ MHz) via frequency doubling and parametric amplification of the weak self-phase modulation (SPM) sidebands in the fundamental spectrum.

Conversely, [15] describes a low-threshold SCG in a random quasi-phase-matched medium (RQPM) [23], a polycrystalline zinc sulfide doped with Cr^{2+} ions [24]. The setup was arranged as a single-pass fs laser amplifier. A 9 mm long Cr:ZnS sample was simultaneously seeded by the mid-IR pulse train (2.4 μm,

3-cycle, 15 nJ at $f_R = 80$ MHz) and optically pumped by continuous wave (CW) radiation from an off-the-shelf Er-doped fiber laser (EDFL). During their propagation through the polycrystalline nonlinear (and laser) medium, mid-IR fs pulses were amplified to about 50 nJ, their spectrum was broadened to an optical octave, and the output pulses were compressed to about 19 fs (2.4 optical cycles). Further, the extended bandwidth of the RQPM process allowed conversion of an octave-spanning mid-IR spectrum to optical harmonics from second (2f) to fourth (4f). A long-wave IR signal, which we attributed to intrapulse difference frequency generation (IDFG), also was detected. High spatiotemporal coherence of the obtained multi-octave continuum was confirmed by the observation of the interference beatings at the carrier envelope offset frequency (f_{CEO}) of the seed laser in the regions of spectral overlap between the adjacent harmonics in 4f–3f, 3f–2f, and 2f–f parts of the continuum.

Here, we report the results of a comprehensive study that has allowed us to identify the dynamics that govern the propagation of few-cycle middle-IR pulses in undoped and transition metal doped polycrystalline ZnS and ZnSe. We perform the study by combining the experiments with the computer simulations. We first characterized the parameters of SCG obtained with a purpose-made polycrystalline Cr:ZnS sample with a variable microstructure. We compared the measured SCG parameters with the simulations based on a realistic model of fs pulse propagation in polycrystalline II-VI semiconductors [25]. We then incorporated into the simulation a model for the laser amplification and the thermal optical effects in the medium. We show that relatively simple assumptions about the laser interactions in an optically pumped polycrystalline Cr:ZnS allow one to achieve a good semi-quantitative agreement between measured and simulated multi-octave spectra. An obtained agreement has encouraged us to make several important predictions about fs SCG in RQPM media. Specifically, we demonstrate that RQPM enables the generation of exceptionally broad coherent spectral distributions that span the whole transparency window of II-VI semiconductors from the bandgap edge to the phonon cutoff. We also show that the control of polycrystalline microstructure enables the control of nonlinear propagation of few-cycle pulses, which can be tuned from conventional self-focusing to CQN-induced self-defocusing.

## 2. Cr:ZnS: PROPERTIES, SAMPLE PREPARATION, AND EXPERIMENTAL RESULTS

Cr:ZnS is a typical representative of a large family of transition-metal-doped II-VI chalcogenides (TM:II-VI) [23]. ZnS is a wideband gap (3.7 eV) semiconductor with a remarkable IR transparency (up to 14 μm) and high second- and third-order nonlinearities (see details in Supplement 1). ZnS doped with Cr^{2+} ions is often referred to as the "Ti:sapphire of the middle IR" due to its broad tuning range (1.8–3.3 μm) and room temperature operation with ~80% quantum efficiency. Cr:ZnS and its sister material, Cr:ZnSe, support all laser regimes, including sub-three-cycle Kerr lens mode-locked oscillators [26,27] and multi-GW chirped pulse amplifiers [28,29] at the mid-IR central wavelength 2.4 μm.

Cr:ZnS is not suitable for birefringent phase matching because of its isotropic zinc-blende structure. However, the

material is available as a polycrystal grown by chemical vapor deposition process (CVD). Polycrystalline Cr:ZnS consists of a multitude of single-crystal grains with a broad distribution of grain sizes and orientations. It has been recently demonstrated that this microstructure is well suited for three-wave mixing of spectrally broad fs pulses via RQMP process [30,31]. Further, within an appropriate range of annealing temperatures, post-grown thermal diffusion doping of CVD-grown ZnS [32] retains the polycrystalline zinc-blend structure of the material. Therefore, ultrafast polycrystalline Cr:ZnS lasers and amplifiers feature nonlinear frequency conversion directly inside their gain elements [33].

Fabrication of polycrystalline Cr:ZnS gain elements with controlled microstructure is illustrated in Fig. 1(a) and is described in detail in [25,31]. In short, we sealed undoped CVD-grown ZnS samples in the contact with metallic chromium in quartz ampoules under 10^{-5} Torr vacuum. Several batches of the samples were annealed at different temperatures (T, from 900 to 1000 °C) for different times ranging from several days to several weeks. A part of the obtained Cr:ZnS samples was used for the material characterization such as measurements of Cr^{2+} concentration and of the grain size distributions. Another part of the Cr:ZnS samples was optically polished and used in the SCG experiments. The most pronounced variation of the microstructure, which was our goal for the purposes of the present study, was achieved for a batch annealed at T = 950°C for 2 weeks. Obtained parameters of a Cr:ZnS sample from this batch are summarized in Fig. 2.

The experimental setup for the SCG characterization is shown in Fig. 1(b). The setup is very similar to the one described in [15]. We used a three-cycle oscillator at 2.4 μm central wavelength with 1.2 W average and 0.5 MW peak
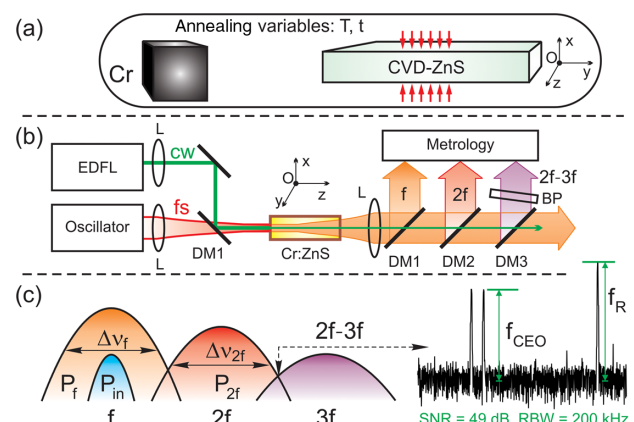
Fig. 1. (a) Preparation of a Cr:ZnS sample (see main text). Red arrows show the direction of Cr diffusion. The sample is statistically uniform in Oy and Oz directions and has variable microstructure on Ox direction. (b) Setup for SCG generation and characterization. L, lenses; DM, dichroic mirrors; and BP, bandpass filter at 870 nm. For simplicity, only the transmissive imaging components (L) are shown; actual setup also included reflective curved mirrors. (c) SCG characterization including the measurements of average power ($P_{in,f,2f}$), spectral bandwidth at −10 dB with respect to the main peak ($\Delta\nu_{f,2f}$), SNRs of rf signals in the 2f–3f band ($f_{R,CEO}$) Power P_{in} is measured at the output of the setup with EDFL inactive, to account for Fresnel losses on the uncoated sample.
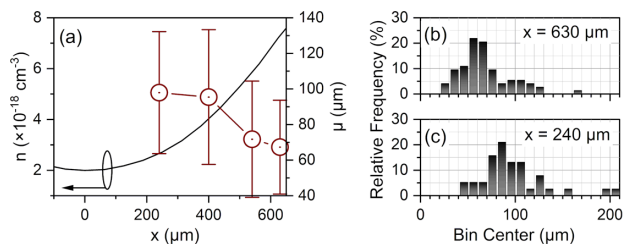
**Fig. 2.** (a) Measured Cr^{2+} concentration (n, left) and average grain size (μ, right) versus location in the Cr:ZnS sample (x); error bars show the dispersion of the grain size distribution σ; x = 0 corresponds to the minimum concentration in the middle of the sample. (b) and (c) Measured distributions of the grain sizes near the surface and in the middle of the sample.

power, $f_R = 80$ MHz, $\Delta\nu_{in} = 14(26)$ THz full width at half-maximum (FWHM) bandwidth of -10 dB. A pulse train from the oscillator was pre-chirped with group delay dispersion (GDD) ≈ -700 fs^2 and superimposed with CW EDFL radiation on a dichroic mirror DM1. The two beams were focused in the uncoated 9 mm long Cr:ZnS sample into ≈ 170 μm and ≈ 60 μm spots, respectively ($1/e^2$ intensity diameter). The importance of input pulses' pre-chirping and of the beam size optimization will be explained in Section 3. The Cr:ZnS sample was installed on an XYZ stage and cooled with room temperature water. The output parameters of the setup were characterized in the range of EDFL powers (0–11 W) and in different locations within the sample along Ox and Oy directions.

Quantitative measurement of SCG spectra over many optical octaves and with a high dynamic range is a cumbersome task. Therefore, we implemented an express-diagnostics scheme shown in Fig. 1(c). We separated f and 2f spectral bands of the continuum with broadband dichroic mirrors to evaluate the laser gain $G = P_f/P_{in}$, the broadening of pulses' spectrum $\Delta\nu_{f,2f}$, and the conversion to second harmonic $\eta_{2f} = P_{2f}/P_f$. We used the optical signal at the wavelength 870 nm to measure the frequencies f_R and f_{CEO} [34]. The signal-to-noise ratio (SNR) of these signals allowed us to evaluate a conversion efficiency to higher harmonics (via f_R) and a degree of spatiotemporal overlap between adjacent harmonics (via f_{CEO}). The metrology equipment included standard power meters, a Thorlabs OSA207C Fourier transform spectrometer, an Acton SP-150 monochromator (for characterization f and 2f spectral bands, respectively), and an Aeroflex 3251 rf spectrum analyzer.

The experimental results are presented in Fig. 3 as functions of x (i.e., the position in the sample along Ox), and of the EDFL power. Here, the displacement of the sample in Ox direction resulted in simultaneous variations of Cr^{2+} ions concentration and of the grain size, as shown in Fig. 2. Cr^{2+} concentration, in turn, defines the laser interactions in the sample: absorption of CW EDFL radiation, amplification of input pulses, and thermal-optical effects in the pumped channel.

Remarkably, the signals acquired in different parts of the continuum exhibit dissimilar behaviors. For instance, optical power in the 2f band follows the laser power in fundamental mid-IR band, as shown in Figs. 3(a) and 3(b). On the other hand, we observed pronounced threshold-like behavior of the nonlinear spectral broadening: small displacement of the crystal [see arrow
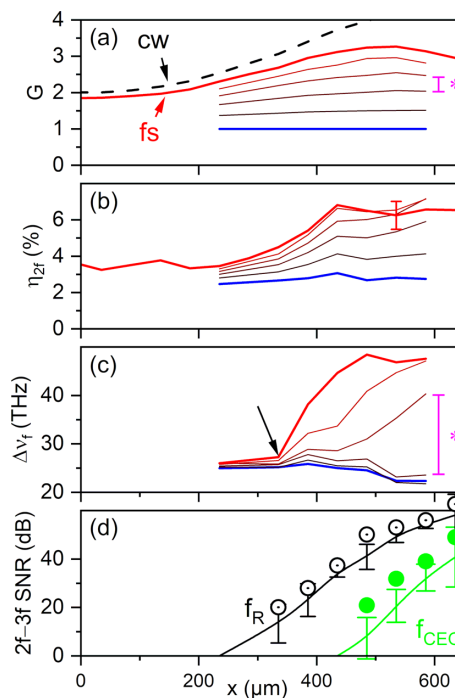
Fig. 3. (a)-(c) Gain (G), SHG conversion efficiency (η_{2f}), and spectral bandwidth ($\Delta\nu_f$) versus location in the sample along Ox direction measured at different levels of EDFA power. Thick red and blue lines correspond to $P_{EDFL} = 11.2$ W and EDFL inactive, respectively; thin lines correspond to the intermediate power levels of 2, 4.2, 6.5, and 9 W. Red bar in (b) shows the dispersion of SHG signal measured in five different points along Oy direction. (d) SNR of the signals at the frequencies f_R (circled dot) and f_{CEO} (green filled circle) versus x. The signals were measured at $P_{EDFL} = 11.2$ W in 5 different points spaced by 50 μm along Oy direction. Symbols show the maximum measured value; solid lines with the error bars show averaged value with the standard deviations (geometric mean).

in Fig. 3(c)] or small increase of the pump power [see asterisks in Figs. 3(a) and 3(c) marking the increments] result in a dramatic enhancement of the fundamental spectral bandwidth.

The optical signals in the 2f–3f band of the continuum exhibit exponential dependences on x at low level of the signals, as shown in Fig. 3(d). However, with an increase in the signal level, the magnitudes of f_R and f_{CEO} signals tend to saturate: f_R signal starts to saturate at x >500 μm, while f_{CEO} signal shows some saturation at x > 600 μm. Similar behavior of the $f_{R,CEO}$ signals during the gradual increase of P_{EDFL} was observed in a separate measurement where the initial exponential growth was followed by some saturation, as illustrated later in Fig. 6.

Figure 3(d) also illustrates the influence of the sample's local microstructure on the conversion to higher optical harmonics. The displacement of our polycrystalline sample along Oy direction exposed the fs pulse train to the different sets of grains (although with similar statistical distributions). Our experiments show that the variation of the local grain distribution may change the f_{CEO} signal by an order magnitude, while the f_R signal is changed by 3–6 dB. It is important to mention that discovery of the "good" locations in the sample that correspond to the highest SNR of the f_{CEO} signal was very straightforward. For instance, Fig. 1(c) illustrates the rf spectrum of f_{CEO} beating in such a good spot. As can be seen, the signal was measured with

rather high SNR = 49 dB in a 200 kHz resolution bandwidth (RBW). Conversely, the dependence of SHG signal on the local grain distribution is much less pronounced: We measured approximately 10% fluctuation during the sample displacement in Oy direction, as shown in Fig. 1(b) by the error bar.

Obtained experimental results, as well as our earlier observations, raise a number of questions about the propagation of few-cycle pulses in optically pumped polycrystalline Cr:ZnS amplifiers. Why, in the first place, is the broadening of the pulse spectrum so strong? Can we control the SCG threshold? What is the extent of nonlinear pulse compression? How does the SCG spectra depend on the microstructure of the sample? In the next section, we give the answers to these questions by comparing the experimental observations to a rigorous numerical modeling.

3. NUMERICAL MODELING OF PULSE PROPAGATION IN POLYCRYSTALLINE Cr:ZnS

To explain the fs SCG in bulk medium at relatively low nJ-level pulse energy, we employ fully resolved, down to subwavelength spatial and subcycle temporal scales, numerical simulations based on the z-propagated unidirectional pulse propagation equation (UPPE) [35,36] with the light–matter interactions implemented as in [25]. A three-dimensional (3D) map of a polycrystalline microstructure is generated using Voronoi tessellation that provides fairly good approximation of experimentally measured spatial distributions in CVD-grown ZnS and ZnSe. Each point of the computational grid is then assigned the corresponding grain orientation and, hence, the nonlinear tensor reflecting the specific local frame of reference aligned with the crystal axes. Thus, the $\chi^{(2)}$ process is resolved with high spatial resolution on a grain-by-grain basis. Further, the model accounts for the third-order nonlinearities and free carrier generation, as well as the spatial and temporal structure of the beam. The details on implementation and material parameters are provided in Supplement 1. Essential for this study is the inclusion of the model of thermal optical effects in the medium. With the help of simulations, we can identify the thermal lensing in Cr:ZnS as the enabling reason for the observed low-threshold supercontinuum generation.

A. Simulation Versus Experimental Results

The thermal optical effects in Cr:ZnS are modeled by imposing a weak waveguide (WG) with a linear index change of $\Delta n = (dn/dT)\Delta T$, where dn/dT is the temperature dependence of the refractive index, and ΔT is the temperature increase induced by pump beam, roughly proportional to the pump power, as described in Supplement 1.

Figure 4(a) illustrates the comparison between simulated and measured spectra, which exhibit a strong influence of thermal effects on spectral evolution. Inclusion of the thermal WG into the simulation allows the reproduction of major qualitative features seen in the experiments. The slight discrepancy around the second and the third harmonic could be explained by the mixing of the EDFL pump with the seed pulse producing the shoulders on the short-wavelength side of the two harmonic bands. Note that by adding a CW background field at $\lambda = 1.6\,\mu m$ in the simulation, we were able to qualitatively capture the additional
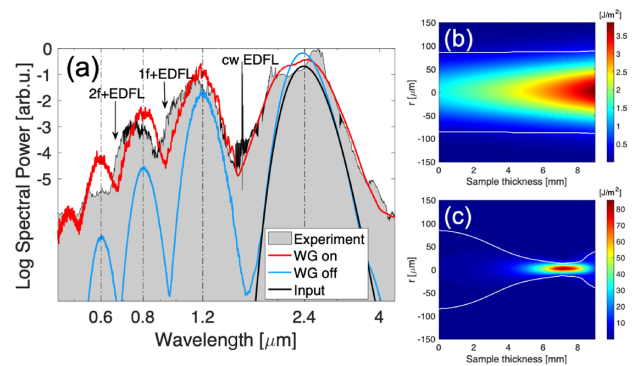

Fig. 4. (a) Experimentally measured supercontinuum versus the simulation-predicted spectra with or without thermal effects in a 9 mm Cr:ZnS sample. (b) Transverse fluence profile of the pulse without inclusion of any thermal effects [corresponds to the blue line in (a). (c) Fluence distribution with a weakly focusing thermal waveguide of $\Delta n = 6 \times 10^{-4}$ included in the simulation, which corresponds to the red line in (a). The white lines indicate the $1/e^2$ beam waist, which has an initial value of 85 μm.

weak blue-shifted broadening. The slight difference can also be explained in part by the fact that doping of ZnS with Cr^{2+} introduces additional absorption between the wavelengths of 0.5–1.5 μm [37], which is ignored in simulations.

Figures 4(b) and 4(c) show that the thermal WG leads to completely different intensity profiles along the propagation direction. Thus, from the results presented in Fig. 4, one may surmise that thermal lensing has changed the interaction dynamics in a substantial way. It allows us to conclude that the thermal WG is the crucial mechanism enabling extreme nonlinear conversion at relatively low (nJ-level) pulse energy. To aid in the interpretation of the results, Fig. 5 shows the effects of the thermal WG and laser gain (G, see Supplement 1) on the fundamental spectral broadening (left) and the second harmonic generation efficiency (right). One can see that a combination of gain, thermal lensing, and the material microstructure gives rise to a SCG threshold: Increasing the pump power in the experiment increases the gain and the focusing power of the thermal WG simultaneously, and this corresponds to moving uphill, roughly in a diagonal direction following a trajectory along the surfaces shown in the figure. Changing the concentration of the laser centers will mostly affect the relative strength of the variations of Δn and G. When the dopant concentration is higher, the trajectory shifts toward the upper-diagonal direction and explains the experimentally observed saturation.

Figure 5 clearly demonstrates that it is the thermal WG that enables the high efficiency of the frequency conversion found in the experiment. For a different crystal structure or lasing condition, there may be correspondingly a different optimal thermal lens. As in simulation predictions, a prominent broadening of the fundamental starts to appear when the pump power is larger than 4 W, and reaches its maximum when it is approximately 8–10 W. The explosive spectral broadening occurs when the thermal focus forms at the exact same position in the crystal, where the pre-chirp is compensated by the material dispersion. In this case, the thermal-lensing helps to reduce the distance needed for the pulse to collapse. Without the thermal effect, the 9 mm distance would not be sufficient for SCG. A further
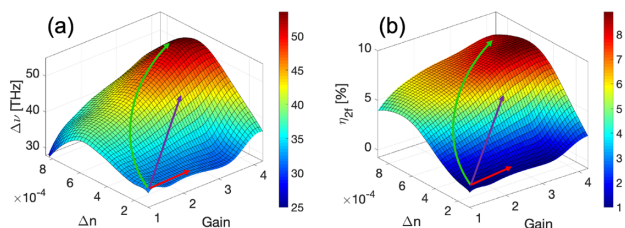
Fig. 5. Simulated (a) fundamental spectral bandwidth at −10 dB level $\Delta\nu$ and (b) SHG efficiency η_{2f} as a function of the laser gain and of the refractive index change imposed by thermal effect Δn. Red, purple, and green arrows indicate qualitative trajectories of increasing pump power and its impact on maximum achievable value of gain, and Δn at low, medium, and high doping level, respectively.

increase of the pump power or of the dopant concentration will only lead to earlier collapse of the pulse, and therefore a narrower supercontinuum is expected. Our simulations also showed that the control of the chirp alone is insufficient in the absence of thermal effects to achieve bandwidths comparable to those seen in the experiments. It is therefore the interplay between the nonlinear and thermal effects that is essential for the broadest supercontinuum spectra.

Figure 6 offers a comparison of trends between the simulations and experiments of the spectral bandwidth of the fundamental and the growth of the optical signal in the region of the spectral overlap between 2f and 3f bands. The startling difference between the spectral broadening in the presence and in the absence of the thermal WG shows that the simulation
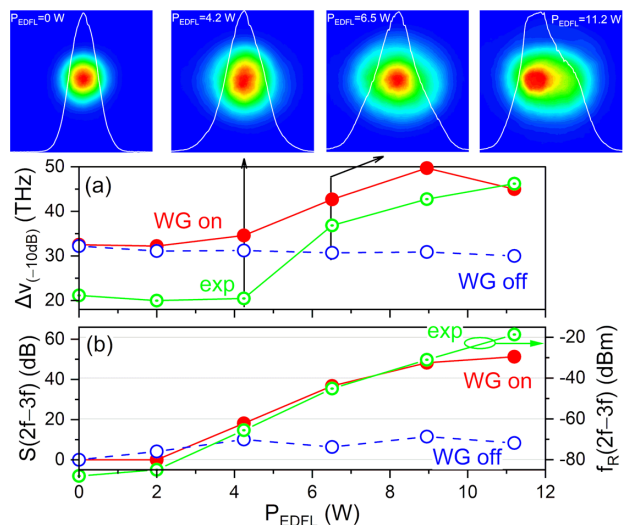
Fig. 6. Measured and simulated parameters of SCG versus CW EDFL power. (a) Fundamental spectral bandwidth at −10 dB with respect to the peak. (b) Levels of the optical signal in the region of spectral overlap between 2f and 3f bands presented on log scale. In both panels, the "WG off" labels (blue circle) correspond to thermal effects being neglected in the simulations, and the "WG on" labels (red filled circle) correspond to a linear growth of ΔT from 0°C to 15°C as pump power increases. The experimental results correspond to x ≈ 600 µm, as shown in Fig. 3. Inserts show measured beam profiles at different levels of EDFL power. Output beam was collimated using a spherical mirror with 100 mm radius. Beam profiles were acquired at ≈2 m distance from the Cr:ZnS sample with a laser beam profiling camera (Spiricon pyrocam, Ophir Optronics Solutions Ltd., Jerusalem). Note that we used a Ge filter to block the NIR part of the continuum.

correctly captures the nature of the threshold-like behavior observed in the experiments. While the relatively smaller bandwidth seen in the experiments at lower powers can be attributed to the absorption by Cr^{2+} centers in the ground state, the explosive growth of the bandwidth with the increase of pump power is clearly captured. The exponential increase of the optical signal in the 2f–3f band is also nicely reproduced.

Figure 6 also allows a comparison of spectral and spatial parameters of output radiation. As can be seen, the onset of supercontinuum at $P_{EDFL} = 6.5$ W transforms the output beam profile to a distinctly non-Gaussian shape. On the other hand, an additional beam characterization in the CW regime of the oscillator (i.e., with the nonlinearities turned off) has confirmed the Gaussian beam profile in the whole range of EDFL powers. Thus, we can tentatively conclude that the nonlinear interactions in Cr:ZnS result in significant modifications of the spatial distribution while the beam divergence is simultaneously influenced by the thermal WG and by the nonlinearities.

It is important to mention that at the current stage, the model of the laser interactions in Cr:ZnS is simplified to a necessary minimum. Therefore, our estimates of the thermal WG parameters on, e.g., Cr^{2+} concentration and on the pump beam parameters are approximate. Yet, obtained results demonstrate that very simple assumptions about the thermal lensing and the laser gain in the medium are sufficient for semi-quantitative predictions of the developed model.

B. Spatiotemporal-Spectral Dynamics in Polycrystalline II-VI Semiconductors

The obtained agreement between experiments and simulations in terms of the fundamental spectral broadening, the efficiency of harmonic generation, and the ability to reproduce the SCG threshold suggests that the model can capture the essential physics, despite some simplifying assumptions. In what follows, we use the model to extend our understanding of the dynamical aspects of the light–matter interaction, to study the properties of the generated radiation, and to map out promising directions of future explorations. For the sake of compactness, we limit our presentation to several interesting aspects of spatial-temporal-spectral dynamics in polycrystalline II-VI semiconductors. Rich polarization dynamics in RQPM media as well as the effects due to the carrier envelope phase (CEP) of input pulses, which are also captured by the model, represent other important research topics and will be reported in subsequent papers.

The spectral width of the fundamental band shown in Fig. 4 supports, theoretically, a pulse duration down to 17 fs. However, this does not automatically imply that a short-duration pulse develops spontaneously. In fact, simulations revealed a more complex situation: Upon the pulse propagation as the material dispersion offsets its pre-chirp, the pulse exhibits a minimal duration of three cycles after 6 mm of propagation, and is subsequently stretched to a FWHM duration of 38 fs at the exit of the sample. Upon numerically adjusting its residual GDD and third-order dispersion (TOD), the fundamental part can be compressed to an optimal duration of 19 fs, as shown in Fig. 7 in the central insert. This result is in a good agreement with the experimental observation: Recompression of mid-IR pulses to about 19 fs was reported in [15].
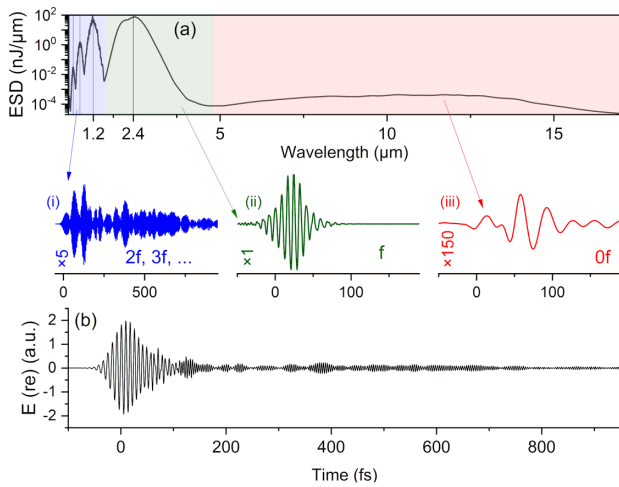
Fig. 7. (a) Simulated spectral and (b) temporal distributions after propagation through a 9 mm polycrystalline ZnS (laser interactions are included as G ≈3 and ΔT = 12°C). The inserts i, ii, and iii show, respectively, temporal profiles of the NIR signal consisting of optical harmonics, fundamental mid-IR signal (after numerical compensation of the second- and the third-order dispersion), and long-wave IR signal (after ≈6 mm propagation, as discussed in the main text). The vertical scales in the inserts i (iii) were magnified by a factor of 5 (150) with respect to the overall waveform (b).

The dynamics of the second-harmonic band is different. It experiences a higher group velocity dispersion (GVD) in the material, which has a twofold influence. On one hand, the recorded high SHG efficiency partially results from the fact that pulse temporal walk-off due to group velocity mismatch prevents the energy from flowing back to the fundamental. On the other hand, the stochastic nature of RQPM creates a random phase variation on each constituent part of the harmonic signal, thus making it almost impossible to compress it as a whole. More details on the generation of optical harmonics in polycrystalline media in a few-optical-cycle regime can be found in [38].

Simulations also reveal the long-wavelength IR (LWIR) signal covering 5–15 μm as a result of IDFG. One remarkable feature is that the temporal evolution of the IDFG signal, as shown in the right insert in Fig. 7, to a large extent, follows the pattern seen in the fundamental band; namely, a single-cycle waveform (39 fs FWHM of intensity distribution) at the central wavelength 10 μm forms at the propagation distance of 6 mm with a conversion efficiency of roughly 0.005%. Later, because of the strong dispersion between 10 and 15 μm, the pulse stretches into picosecond duration, while the conversion efficiency increases to about 0.1%. This behavior is in contrast to that seen for second and higher harmonic bands, as shown in the left insert in Fig. 7.

Thus, our simulations suggest that not only is there a non-negligible generation of a long-wavelength radiation, but also that it may inherit favorable coherence properties such as compressibility from the well-behaved fundamental. Therefore, a further study of IDFG in polycrystalline II-VI semiconductors (e.g., an exploration of the energy scaling capabilities in a single-cycle regime), represents an interesting topic of future research.

Another intriguing aspect of fs pulse propagation in $\chi^{(2)}$ media is the coupling of cascaded quadratic nonlinearities to spatial-temporal-spectral dynamics. CQN contributes to a total effective nonlinear index of the medium as $n_{2,\text{eff}} = n_2 - n_{2,\text{CQN}}$. The control of spatial dynamics in $\chi^{(2)}$ single crystals is relatively well understood [12]: The sign and the magnitude of $n_{2,\text{eff}}$ can be manipulated by control of the phase mismatching parameter Δk (e.g., using the crystal's birefringence). More recently, simple and elegant semi-analytical models were developed to engineer spatial dynamics of multicycle pulses in QPM structures [16]. Conversely, the propagation of few-cycle pulses in RQPM media results in simultaneous phase-mismatched three-wave mixings over several optical octaves. This makes CQN in polycrystals more intricate and subtle (and hence very challenging for the analytical study of simplified numerical methods). Here, we deploy our rigorous model to carry out the first study of CQN in polycrystalline II-VI semiconductors.

We wish to examine the effect of CQN in two different cases. In scenario A, which is relevant for optical frequency comb applications [33], an incident 45 nJ pulse at the central wavelength of 2.4 μm propagates through the 9 mm ZnS crystal with different average grain sizes, as compared to the case of $\chi^{(2)}$ being switched off. The initial pulse has an unchirped duration of 24 fs, and a $1/e^2$ intensity radius of 85 μm. In scenario B, which is relevant for, e.g., high-gain fs amplifiers [23,25], an incident 2 μJ pulse with an initial duration of 60 fs, and a $1/e^2$ intensity radius of 60 μm at the central wavelength of 3.6 μm propagates through a 2.5 mm thick ZnSe crystal. The left panels of Fig. 8 show the evolution of beam radial sizes, and the right panels show the strongest contrast of peak intensity difference seen in numerical experiments. The spatial evolutions correspond to a superposition of the decreasing fundamental and growing harmonics. Our additional analysis has shown that the fundamental components diverge somewhat stronger than the whole signal. However, at least for scenario A, the changes are minor and do not alter the ranking of the curves.

It can be seen that even at lower energy and second-order nonlinearity of scenario A, CQN significantly alters the evolution of fs pulses: The beam divergence in RQPM medium is stronger than that in a pure $\chi^{(3)}$ medium. Further, depending on the average grain size, fs pulses may diverge even stronger than a reference Gaussian beam with low intensity. Thus, the quadratic process in polycrystals can completely offset the self-focusing nonlinearity [see the curve corresponding to 20 μm grain in Fig. 8(a)]. The obtained difference in the peak intensity at the exit plane of the pure $\chi^{(3)}$ medium [Fig. 8(b)] and self-defocusing medium [Fig. 8(c)] is approximately 12%, of which up to 7% may be attributed to the conversion to higher harmonics. The self-defocusing effect becomes more prominent in the second scenario with a stronger nonlinearity and a higher intensity. The lower panels in Fig. 8 show that CQN helps the beam to maintain nearly constant size along propagation, avoiding a strong collapse [compare Figs. 8(e) and 8(f)]. Obtained results illustrate a few common features of CQN (also seen in single crystals [13,14]): (1) The magnitude of self-defocusing effect is strongly related to the conversion to second harmonic; and (2) small-scale formation of hot spots may happen along with the increase in the whole-beam radius.
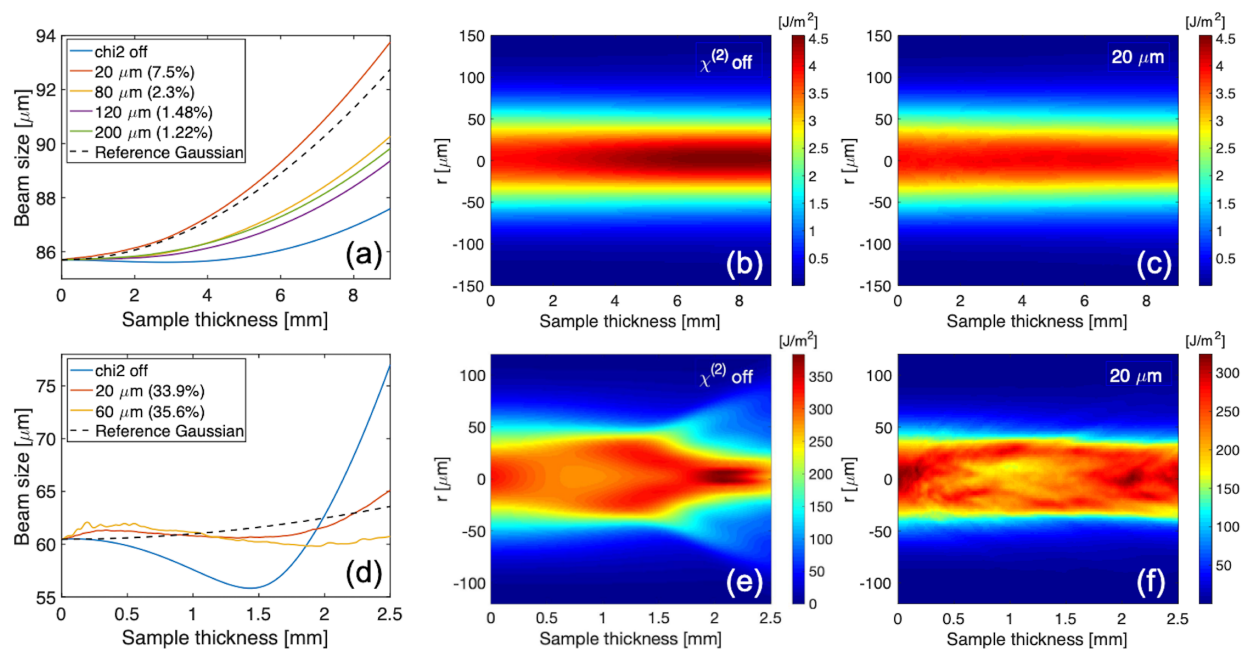
Fig. 8. (a) and (d) Simulated evolution of beam sizes and (b), (c), (e), and (f) the corresponding spatial distribution of fluence in ZnS (first row) and in ZnSe (second row) as a function of sample thicknesses and average grain sizes. The evolutions are shown for all frequency components (fundamental and harmonics). The numbers in the parentheses in the (a) and (d) indicate cumulative conversion to harmonics at the output of the samples. Dashed curves in (a) and (d) correspond to the linear propagations of Gaussian beams with low power. The beam sizes in (a) and (d) are calculated as the second moment width of the intensity distribution.

Thus, our realistic simulations allow us to conclude that the value and even the sign of $n_{2,\text{eff}}$ can be controlled by the modification of polycrystalline microstructure. However, it is important to point out the essential differences between CQN in RQPM media and CQN in single crystals (or in QPM materials with a well-defined microstructure). In single crystals and in the case of multicycle pulses, the parameter $n_{2,\text{CQN}}$ can be derived from a natural conversion and back-conversion cycle between the fundamental and the second harmonic [12,39]. In QPM media, the $n_{2,\text{CQN}}$ can be engineered by the control of the QPM grating vector values [16]. Conversely, in RQPM media, CQN is defined by a random walk of the phase relations between the fundamental and harmonics. Further, in a few-cycle regime, the conversion and back-conversion cycle is being cut off; hence, the strength of CQN is being affected by the f-2f temporal walk-off. It is therefore possible that the effective value of $n_{2,\text{CQN}}$ in polycrystals should also reflect the pulse duration besides the parameters of the medium. We trust that empirical formulae describing CQN in polycrystalline ZnS and ZnSe can be constructed with the help of comparative simulations, but such a project is beyond the scope of this work.

Nevertheless, we expect that self-defocusing nonlinearity in irregular $\chi^{(2)}$ media is a universal effect, which will be eventually observed in other polycrystalline dielectrics and semiconductors. Obtained results suggest that self-defocusing quadratic nonlinearities must be taken into account during the experimental characterization of polycrystals and ceramics: self-defocusing can, e.g., affect the z-scan measurements. Our simulations also show a significant dependence of self-defocusing on the microstructure of the material. Importantly, we observe a nonlinear dependence of the self-defocusing effect

on the average grain size in ZnS and ZnSe polycrystals, as shown in Fig. 8(a). Further, maximum self-defocusing does not necessarily correspond to the highest level of second harmonic, as shown in Fig. 8(d). Thus, the engineering of grain microstructures in polycrystals provide interesting—and yet to be explored—opportunities for the control of fs pulse propagation.

4. CONCLUSION

In conclusion, we introduce what we believe is a new class of fs SCG in bulk media where the nonlinear spectral broadening and pulse compression is assisted by optical gain and further enabled by a thermal lens, both induced by the CW pump radiation co-propagating with the fs pulse train. This SCG regime combines, to some extent, the advantages of bulk and confined geometries. Similar to waveguide-based setups, it allows for the generation of super-octave coherent spectra at nJ-level pulse energies and at full repetition rates of fs oscillators. At the same time, the spatial-and-temporal dynamics akin to those in bulk media are central to the favorable properties of the fs SCG.

We also introduce a simple and reproducible experimental technique for optimization of this low-threshold bulk SCG. The technique is based on a polycrystalline Cr:ZnS with a variable microstructure (concentration of Cr^{2+} centers and grain size). When such a sample is used as a gain element in an optically pumped single-pass fs amplifier, translations of the sample with respect to the laser beams allow optimization of the interplay between various effects influencing fs pulse propagation in the material.

The advantages of the low-threshold SCG in polycrystalline Cr:ZnS and Cr:ZnSe are numerous. The scheme is simple in

implementation and, hence, robust: SCG is achieved by a loose focusing of two superimposed laser beams into a miniature Cr:ZnS sample. The input pulse train is simultaneously amplified to a few watts, broadened to an octave and compressed to two cycles. Generation of optical harmonics in the polycrystalline sample allows for the direct detection of the oscillator's f_{CEO} with a high SNR. Last, but not least, the proposed scheme provides direct access to the mid-IR range 2–3 µm, and it is power scalable [40] and compatible with new techniques for few-cycle lasing and frequency comb generation in the long-wave infrared [41,42].

The experimental study of SCG in optically pumped polycrystalline Cr:ZnS was carried out in parallel with computer simulations based on the recently developed realistic models. We demonstrate that the inclusion in the model of just two additional parameters—amplifier's gain G and the temperature increase ΔT—results in semi-quantitative agreement between the measured and simulated spectral and temporal distributions.

On the other hand, we show that now available Maxwell-level $(3+1)$D models are uniquely suited for quantitative studies of complex interplays between various nonlinear effects inside polycrystalline II-VI semiconductors. First and foremost, the simulations allow us to assert that fs pulse propagation in $\chi^{(2)}$ polycrystalline media (in the absence of thermal optical effects) is strongly affected by the self-defocusing nonlinearities arising from intrapulse three-wave mixings during the RQMP process. Our realistic model predicts that polycrystalline ZnS and ZnSe feature self-defocusing nonlinearity in a broad range of pulse energies, from nJ to µJ level. Importantly, the control of the polycrystalline microstructure (i.e., of the average grain size) allows control of the magnitude and the sign of effective Kerr lens in the medium.

Further, our simulations reveal that polycrystalline ZnS and ZnSe can be used to generate single-cycle electromagnetic transients in the important long wave IR part of the spectrum via optical rectification. The predicted IDFG efficiency is non-negligible even at nJ-level energy of input pulses. For instance, according to the simulations, an optically pumped polycrystalline Cr:ZnS amplifier seeded by a 15 nJ pulse train at the $f_R = 80$ MHz features $\approx 10^{-4}$ conversion to the long wave IR transients that corresponds to 0.3 mW power. This is a level already sufficient for some applications in spectroscopy, in particular in frequency comb spectroscopy with conventional square-law detectors as well as with electro-optic sampling [43]. In our opinion, the obtained experimental and computational results open several new avenues of research and development related to the engineering of spatial-spectral-temporal effects in lasers, amplifiers, and nonlinear-frequency conversion devices based on polycrystalline ZnS and ZnSe.

Supplemental document. See Supplement 1 for supporting content.

REFERENCES

1. R. R. Alfano, *The Supercontinuum Laser Source* (Springer-Verlag, 2016).
2. S. A. Diddams, "The evolving optical frequency comb [Invited]," J. Opt. Soc. Am. B **27**, B51–B62 (2010).
3. A. Wirth, M. T. Hassan, I. Grguraš, J. Gagnon, A. Moulet, T. T. Luu, S. Pabst, R. Santra, Z. A. Alahmed, A. M. Azzeer, V. S. Yakovlev, V. Pervak, F. Krausz, and E. Goulielmakis, "Synthesized light transients," Science **334**, 195–200 (2011).
4. X. Feng, S. Gilbertson, H. Mashiko, H. Wang, S. D. Khan, M. Chini, Y. Wu, K. Zhao, and Z. Chang, "Generation of isolated attosecond pulses with 20 to 28 femtosecond lasers," Phys. Rev. Lett. **103**, 183901 (2009).
5. A. L. Gaeta and R. S. Windeler, "Microstructure fiber and white light generation," in *Femtosecond Optical Frequency Comb: Principle, Operation, and Applications* (Kluwer Academic/Springer, 2005), pp. 97–111.
6. J. M. Dudley, G. Genty, and S. Coen, "Supercontinuum generation in photonic crystal fiber," Rev. Mod. Phys. **78**, 1135–1184 (2006).
7. N. Nagl, K. F. Mak, Q. Wang, V. Pervak, F. Krausz, and O. Pronin, "Efficient femtosecond mid-infrared generation based on a Cr:ZnS oscillator and step-index fluoride fibers," Opt. Lett. **44**, 2390–2393 (2019).
8. Y. Okawachi, M. Yu, J. Cardenas, X. Ji, A. Klenner, M. Lipson, and A. L. Gaeta, "Carrier envelope offset detection via simultaneous supercontinuum and second-harmonic generation in a silicon nitride waveguide," Opt. Lett. **43**, 4627–4630 (2018).
9. D. Martyshkin, V. Fedorov, T. Kesterson, S. Vasilyev, H. Guo, J. Liu, W. Weng, K. Vodopyanov, T. J. Kippenberg, and S. Mirov, "Visible-near-middle infrared spanning supercontinuum generation in a silicon nitride (Si_3N_4) waveguide," Opt. Mater. Express **9**, 2553–2559 (2019).
10. A. Dubietis, G. Tamošauskas, R. Šuminas, V. Jukna, and A. Couairon, "Ultrafast supercontinuum generation in bulk condensed media," Lith. J. Phys. **57**, 113–157 (2017).
11. A. Ostrovskii, "Self-action of light in crystals," Pis'ma Zh. Eksp. Teor. Fiz. **5**, 331 (1967) [JETP Lett. 5, 272–275 (1967)].
12. B. Zhou and M. Bache, "Invited Article: Multiple-octave spanning mid-IR supercontinuum generation in bulk quadratic nonlinear crystals," APL Photon. **1**, 050802 (2016).
13. F. W. Wise and J. Moses, "Self-focusing and self-defocusing of femtosecond pulses with cascaded quadratic nonlinearities," in *Self-focusing: Past and Present* (Springer, 2009), pp. 481–506.
14. X. Liu, L. Qian, and F. Wise, "High-energy pulse compression by use of negative phase shifts produced by the cascade $\chi^{(2)}$ nonlinearity," Opt. Lett. **24**, 1777–1779 (1999).
15. S. Vasilyev, I. Moskalev, V. Smolski, J. Peppers, M. Mirov, V. Fedorov, D. Martyshkin, S. Mirov, and V. Gapontsev, "Octave-spanning Cr:ZnS femtosecond laser with intrinsic nonlinear interferometry," Optica **6**, 126–127 (2019).
16. A. S. Mayer, C. R. Phillips, and U. Keller, "Watt-level 10-gigahertz solid-state laser enabled by self-defocusing nonlinearities in an aperiodically poled crystal," Nat. Commun. **8**, 1673 (2017).
17. R. Šuminas, G. Tamošauskas, V. Jukna, A. Couairon, and A. Dubietis, "Second-order cascading-assisted filamentation and controllable supercontinuum generation in birefringent crystals," Opt. Express **25**, 6746–6756 (2017).

18. R. Šuminas, A. Marcinkevičiūtė, G. Tamošauskas, and A. Dubietis, "Even and odd harmonics-enhanced supercontinuum generation in zinc-blende semiconductors," J. Opt. Soc. Am. B **36**, A22–A27 (2019).

19. A. J. Lind, A. Kowligy, H. Timmers, F. C. Cruz, N. Nader, M. C. Silfies, T. K. Allison, and S. A. Diddams, "Mid-infrared frequency comb generation and spectroscopy with few-cycle pulses and $\chi^{(2)}$ nonlinear optics," Phys. Rev. Lett. **124**, 133904 (2020).

20. M. Rutkauskas, A. Srivastava, and D. T. Reid, "Supercontinuum generation in orientation-patterned gallium phosphide," Optica **7**, 172–175 (2020).

21. M. Jankowski, C. Langrock, B. Desiatov, A. Marandi, C. Wang, M. Zhang, C. R. Phillips, M. Lončar, and M. M. Fejer, "Ultrabroadband nonlinear optics in nanophotonic periodically poled lithium niobate waveguides," Optica **7**, 40–46 (2020).

22. Y. Okawachi, M. Yu, B. Desiatov, B. Y. Kim, T. Hansson, M. Lončar, and A. L. Gaeta, "Chip-based self-referencing using integrated lithium niobate waveguides," Optica **7**, 702–707 (2020).

23. M. Baudrier-Raybaut, R. Haidar, P. Kupecek, P. Lemasson, and E. Rosencher, "Random quasi-phase-matching in bulk polycrystalline isotropic nonlinear materials," Nature **432**, 374–376 (2004).

24. S. Mirov, I. Moskalev, S. Vasilyev, V. Smolski, V. Fedorov, D. Martyshkin, J. Peppers, M. Mirov, A. Dergachev, and V. Gapontsev, "Frontiers of mid-IR lasers based on transition metal doped chalcogenides," IEEE J. Sel. Top. Quantum Electron. **24**, 1601829 (2018).

25. J. Gu, M. G. Hastings, and M. Kolesik, "Simulation of harmonic and supercontinuum generation in polycrystalline media," J. Opt. Soc. Am. B **37**, 1510–1517 (2020).

26. S. Vasilyev, I. Moskalev, M. Mirov, V. Smolski, S. Mirov, and V. Gapontsev, "Ultrafast middle-IR lasers and amplifiers based on polycrystalline Cr:ZnS and Cr:ZnSe," Opt. Mater. Express **7**, 2636–2650 (2017).

27. S. Vasilyev, I. Moskalev, V. Smolski, J. Peppers, M. Mirov, Y. Barnakov, V. Fedorov, D. Martyshkin, S. Mirov, and V. Gapontsev, "Kerr-lens mode-locked Cr:ZnS oscillator reaches the spectral span of an optical octave," Opt. Express **29**, 2458–2465 (2021).

28. Y. Wu, F. Zhou, E. W. Larsen, F. Zhuang, Y. Yin, and Z. Chang, "Generation of few-cycle multi-millijoule 2.5 µm pulses from a single-stage Cr^{2+}:ZnSe amplifier," Sci. Rep. **10**, 7775 (2020).

29. V. E. Leshchenko, B. K. Talbert, Y. H. Lai, S. Li, Y. Tang, S. J. Hageman, G. Smith, P. Agostini, L. F. DiMauro, and C. I. Blaga, "High-power few-cycle Cr:ZnSe mid-infrared source for attosecond soft x-ray physics," Optica **7**, 981–988 (2020).

30. Q. Ru, N. Lee, X. Chen, K. Zhong, G. Tsoy, M. Mirov, S. Vasilyev, S. B. Mirov, and K. L. Vodopyanov, "Optical parametric oscillation in a random polycrystalline medium," Optica **4**, 617–618 (2017).

31. J. Zhang, K. Fritsch, Q. Wang, F. Krausz, K. F. Mak, and O. Pronin, "Intra-pulse difference-frequency generation of mid-infrared (2.7–20 µm) by random quasi-phase-matching," Opt. Lett. **44**, 2986–2989 (2019).

32. S. B. Mirov and V. V. Fedorov, "Mid-IR microchip laser: ZnS:Cr^{2+} laser with saturable absorber material," U.S. Patent6960486-B2 (1November 2005).

33. S. Vasilyev, I. Moskalev, M. Mirov, V. Smolski, S. Mirov, and V. Gapontsev, "Mid-IR Kerr-lens mode-locked polycrystalline Cr:ZnS and Cr:ZnSe lasers with intracavity frequency conversion via random quasi-phase-matching," Proc. SPIE **9731**, 97310B (2016).

34. S. Vasilyev, V. Smolski, J. Peppers, I. Moskalev, M. Mirov, Y. Barnakov, S. Mirov, and V. Gapontsev, "Middle-IR frequency comb based on Cr:ZnS laser," Opt. Express **27**, 35079–35087 (2019).

35. M. Kolesik and J. V. Moloney, "Nonlinear optical pulse propagation simulation: From Maxwell's to unidirectional equations," Phys. Rev. E **70**, 036604 (2004).

36. J. Andreasen and M. Kolesik, "Nonlinear propagation of light in structured media: Generalized unidirectional pulse propagation equations," Phys. Rev. E **86**, 036706 (2012).

37. J. Peppers, V. V. Fedorov, and S. B. Mirov, "Mid-IR photoluminescence of Fe^{2+} and Cr^{2+} ions in ZnSe crystal under excitation in charge transfer bands," Opt. Express **23**, 4406–4414 (2015).

38. J. Gu, A. Schweinsberg, L. Vanderhoef, M. Tripepi, A. Valenzuela, C. Wolfe, T. R. Ensley, E. Chowdhury, and M. Kolesik, "Random quasi-phase-matching in polycrystalline media and its effects on pulse coherence properties," Opt. Express **29**, 7479–7493 (2021).

39. K. Beckwitt, F. W. Wise, L. Qian, L. A. Walker, and E. Canto-Said, "Compensation for self-focusing by use of cascade quadratic nonlinearity," Opt. Lett. **26**, 1696–1698 (2001).

40. I. Moskalev, S. Mirov, M. Mirov, S. Vasilyev, V. Smolski, A. Zakrevskiy, and V. Gapontsev, "140 W Cr:ZnSe laser system," Opt. Express **24**, 21090–21104 (2016).

41. S. Vasilyev, I. S. Moskalev, V. O. Smolski, J. M. Peppers, M. Mirov, A. V. Muraviev, K. Zawilski, P. G. Schunemann, S. B. Mirov, K. L. Vodopyanov, and V. P. Gapontsev, "Super-octave longwave mid-infrared coherent transients produced by optical rectification of few-cycle 2.5-µm pulses," Optica **6**, 111–114 (2019).

42. Q. Ru, T. Kawamori, P. G. Schunemann, S. Vasilyev, S. B. Mirov, and K. L. Vodopyanov, "Two-octave-wide (3–12 µm) mid-infrared frequency comb produced as an optical subharmonic in a nondispersive cavity," Opt. Lett. **46**, 709–712 (2021).

43. A. S. Kowligy, H. Timmers, A. J. Lind, U. Elu, F. C. Cruz, P. G. Schunemann, J. Biegert, and S. A. Diddams, "Infrared electric field sampled frequency comb spectroscopy," Sci. Adv. **5**, eaaw8794 (2019).